

# Space and Time Behavior of Seismic Activity at Mt. Vesuvius Volcano, Southern Italy

by Aldo Zollo, Warner Marzocchi, Paolo Capuano, Anthony Lomax, and Giovanni Iannaccone

**Abstract** We analyze the space and time behavior of seismicity at Mt. Vesuvius during the last 20 yr to characterize the seismic regime of the volcano during the present quiescent period. The new results on the volcano structure inferred from active seismic tomography experiments, the newly implemented 10-yr arrival time catalog, and a high-quality digital waveform data set have been analyzed. The background seismicity is concentrated near and beneath the Mt. Vesuvius crater, with depths lying above and below the discontinuity, which marks the transition from the shallow alluvium/volcanic sediments and the Mesozoic carbonate basement. The focal mechanisms of microearthquakes show variable stress-axis orientations as a function of depth, although there is evidence for a clustering around roughly the north–south to vertical directions for the tension axes and east–southeast–west–northwest to vertical directions for the pressure axes. The statistical analysis of the seismic catalog confirmed the tendency of background seismicity to cluster in time, according to a trigger model (as denoted by Vere-Jones and Davies, 1966), that is, the generalized Poisson process. A significant increase of the average seismic energy release with time is observed, which is related to the occurrence of several  $M_D > 3$  events in the past 10 yr, accompanied by intense swarm activity. This is consistent with the decrease of the  $b$ -value from about 2 to 1 during the same period. The ( $M_D > 3$ ) events are located in the same area and depth range of the whole seismicity, and their fault-plane solutions also show variable stress-axis and nodal-plane orientations. In particular, the moment tensor inversion of  $P$  and  $S$  waveforms from the largest earthquake in the catalog ( $M_D$  3.6, on 9 October 1999) shows no significant departure from a pure shear, double-couple mechanism, thus suggesting a dominant tectonic-like fracture mechanism.

The decrease of parameter  $b$  with time is interpreted as a dominant effect of fluid pressure variations on the present seismic regime at Mt. Vesuvius, which could be driven by the progressive cooling of the volcanic system.

## Introduction

Mt. Vesuvius is located in a densely urbanized corridor along the Bay of Naples and 15 km east of the city of Naples, which has a population of about 2 million. The region has experienced devastating volcanic eruptions during the past 2000 yr, the largest of which totally destroyed the town of Pompei in A.D. 79. This eruption is detailed in the chronicle of Plinius the Elder.

After several centuries of quiescence, the eruptive activity at Mt. Vesuvius resumed in 1631 with a large subplinian eruption (Scandone *et al.*, 1993). The period that followed was characterized by lava flows (Strombolian) with about 15 eruption cycles between 1631 and 1944, each lasting between 2 and 37 yr, with repose periods of 0.5–5.5 yr between cycles (Scandone *et al.*, 1993). Since 1944, the vol-

cano has been dormant with no eruptions but has shown continuous fumarole and moderate seismic activity. There is some concern that this relatively long quiescence since 1944 may be a precursor to a subplinian event, as with the 1631 eruption (see for instance Santacroce, 1991). In fact, the emergency plan prepared by the Ministry of Civil Protection assumes the eruption of 1631 as a reference scenario for the next eruption.

However, because the historical data are not complete enough to characterize the processes that generate, or, at least, precede the volcanic eruptions, much current effort is dedicated to complementary geophysical studies. In this respect, for example, a number of geophysical studies have been performed recently in the area with the goal of imaging

the volcano structure and identifying its feeding system (Zollo *et al.*, 1996, 2002; Di Maio *et al.*, 1998; Gasparini and TomoVes Working Group, 1998; Müller *et al.*, 1999). The main results of the Mt. Vesuvius seismic tomography project (TomoVes Project, Gasparini and TomoVes Working Group, 1998) are detailed images of the shallow volcanic structure and the Campanian Plain and evidence for a 8- to 10-km-deep midcrustal discontinuity associated with an extended molten or partially molten zone (Zollo *et al.*, 1996; Auger *et al.*, 2001).

In addition, Lomax *et al.* (2001), starting from the available 2D velocity profiles produced through the inversion of TomoVes active seismic travel-time data, reconstructed a 3D model of the Mt. Vesuvius area. This model is used for earthquake location and fault mechanism estimates and as a preliminary model for 3D inversions.

The temporal evolution of a volcanic system is established through the surveillance of many parameters, the most important of which is seismic activity. It is important not only because of the insight it provides into magmatic intrusion processes, but also because of the availability of large data sets for many eruptions. The number of seismic indicators is large, the most important ones being the rate of occurrence, the rate of energy release, the trend of the  $b$ -value, hypocentral locations, focal mechanisms, and the occurrence rate of low-frequency and tremor events. In spite of their importance, data relative to hypocentral migration and to the detection of low-frequency volcanic earthquakes are scarce; only in recent years dense seismograph networks have been deployed to monitor the volcanic seismicity. Although less informative, the rate of seismicity and the earthquake magnitudes (and the derived energy release) are usually considered as robust seismic indicators of magma intrusion. Abrupt changes of these seismic parameters occurred from several weeks to months before the largest volcanic eruptions of the last 20 yr (see, for example, the eruptions of Mt. St. Helens, Pinatubo, and Mt. Spurr) (Mc Nutt, 1996).

The present quiescent state of Vesuvius since 1944 is characterized by a low level of seismicity (about several hundred events per year) with mostly earthquakes having a magnitude  $M$  less than 3. The earthquakes are mainly located beneath the crater area at very shallow depths ( $<5$  km). The most energetic earthquakes ( $M > 3$ ) have occurred in the last decade, the strongest of which, a  $M_D$  3.6 event, took place on 9 October 1999. This event was felt throughout the area surrounding the volcano and in the city of Naples, creating alarm among the population and much media attention.

The aim of this article is to provide a detailed description of the recent seismicity at Mt. Vesuvius, which we consider as a reference state for a quiescent phase of the volcano.

The detailed 3D structure of the Vesuvius obtained by the TomoVes seismic tomography studies allows us to re-examine the seismic activity in order to update the models used for describing the space and time of earthquake occurrence at Vesuvius. In this article, based on the earthquake

records of the last 20 yr and more recent high-quality waveform data sets, we recompute the hypocenter locations and the source mechanisms using the new images of the 3D volcano structure, and we analyze and model the space and time occurrence of seismicity at Vesuvius.

### Eruptive History and Structural Features of Mt. Vesuvius

Somma–Vesuvius is a composite volcano complex formed by an older volcano (Mt. Somma) and a young, inner crater (Mt. Vesuvius). The oldest outcropping volcanic deposits date back to about 25,000 yr B.P. Mt. Somma is essentially formed by lavas, and its morphology is the result of several collapse events that resulted in the formation of a summit caldera.

Mt. Vesuvius is part of a volcanic field located within a grabenlike structure bordered by Mesozoic limestones. The volcanic field includes the Campi Flegrei caldera and the Roccamonfina stratovolcano (Fig. 1). The graben developed during the Pleistocene, and it was filled with marine and fluvial sediments interlayered with volcanic products. Volcanic activity in the Bay of Naples started about 120 k.y.

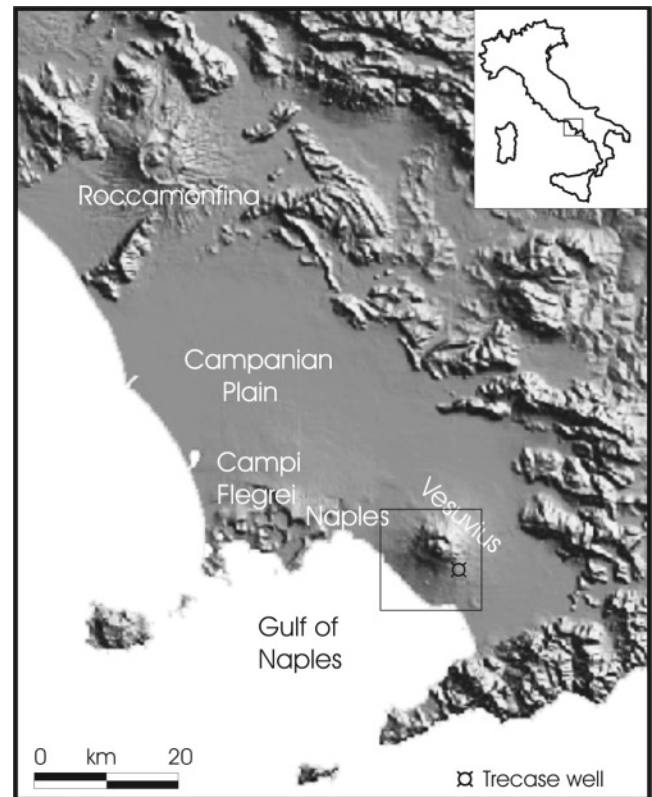


Figure 1. Topographic map of the Campanian Plain region showing the main volcanoes of the area: Vesuvius and Campi Flegrei around the city of Naples and Roccamonfina on the northern part. On the southern flanks of Vesuvius the Trecase well location is shown.

ago. A major ignimbrite eruption occurred 35–39 k.y. B.P. giving rise to a thick deposit (Campanian Ignimbrite) that extends throughout the Campanian Plain.

The Mt. Vesuvius edifice is entirely built on the Campanian ignimbrite and is therefore younger than 35 k.y. During the past 20 k.y., Mt. Vesuvius has produced seven Plinian eruptions at intervals of several thousands of years. The last one occurred in A.D. 79. Each Plinian eruption produced between 5 and 11 km<sup>3</sup> of pyroclastic rocks, which devastated an area of 20,000–30,000 hectares. The summit caldera of Mt. Somma was formed as a consequence of these eruptions (Arnò *et al.*, 1987).

Although the activity of Mt. Vesuvius during Roman times and the Middle Ages is not well documented, information about the occurrence of a major explosive eruption in A.D. 472 and less-violent eruptions around A.D. 511 and 1139 is available. Mt. Vesuvius seems to have been dormant from A.D. 1139 to 1631, when it erupted violently. From 1631 to 1944, it was in almost continuous eruption with strombolian activity producing mostly leucite-tephritic lavas, which cap the south-southeast sector of the volcano edifice.

Since 1944 Mt. Vesuvius had no activity beyond some fumaroles in the crater area and moderate low-magnitude seismicity (maximum magnitude  $M_D$  3.6).

The main information about the shallow structure of the volcano comes from a deep borehole drilled on the southeast slope of Mt. Vesuvius during the 1970s. This well penetrates the entire volcanic sequence reaching the Mesozoic limestone rocks at a depth of about 2200 m (Fig. 2) (Principe *et al.*, 1987). A seismic reflection survey at sea carried out in the Bay of Naples in the early 1970s identified a west-northwest-deepening strong reflector that was interpreted as the top of the Mesozoic limestones (Finetti and Morelli, 1974). The depth and shape of the limestone top beneath Mt. Vesuvius has been inferred by Bouguer anomalies calibrated with the offshore seismic reflection data and the borehole data. Bruno *et al.* (1998) recently mapped the limestone top around Mt. Vesuvius using migrated reflection data by Azienda Generale Italiana Petroli (AGIP). A large, positive magnetic anomaly centered on the volcano edifice is observed from a regional aeromagnetic survey; this anomaly is attributed to the high magnetic susceptibility of volcanic rocks, maybe representing the intrusive solidified core of Mt. Vesuvius (Cassano and La Torre, 1987; Fedi *et al.*, 1998).

Recently, refined images of the shallow (up to 3–4 km depth) structure of Mt. Vesuvius and Campanian Plain are based on data from the TomoVes active seismic experiments performed in the area in 1994, 1996, and 1997 (Zollo *et al.*, 1996, 2000, 2002; Gasparini *et al.*, 1998; De Matteis *et al.*, 2000). The resulting images of Mt. Vesuvius volcano show variable  $P$  velocities in the range 1700–5800 m/sec and fairly detailed image of the top of the Mesozoic carbonate rocks forming the basement of the volcanic area. The limestone top generally dips from the edges of the Campanian Plain toward the volcano, consistent with the Bouguer anom-

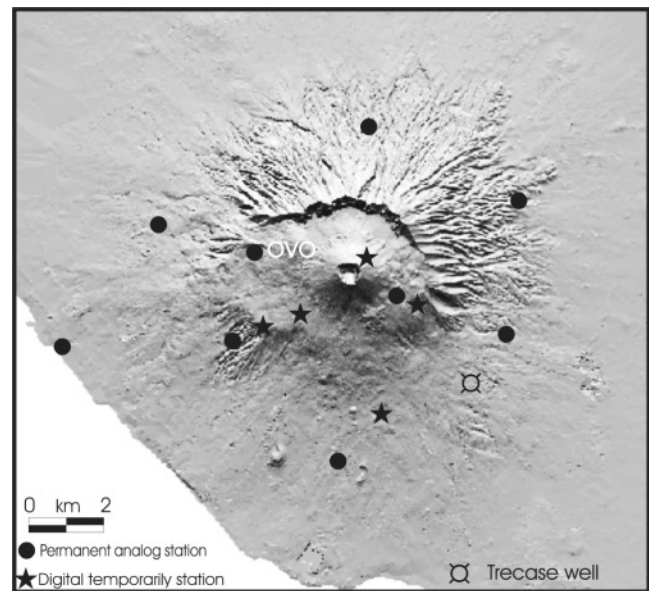


Figure 2. Topographic map of the Mount Vesuvius showing location of permanent and temporary seismic networks managed by Osservatorio Vesuviano.

alies pattern. This Mesozoic surface is apparently continuous under the volcano (Zollo *et al.*, 2002).

The results show a 9-km-long, 1-km-deep east–west-trending depression in the limestone surface on the north side of the volcano, beneath the northeastern border of the Mt. Somma caldera. The presence of a shallow high-velocity body located under the Mt. Somma caldera is indicated both by first  $P$ -wave arrival and reflected  $P$ -wave arrival; this body is interpreted as a subvolcanic or paleovolcanic structure (Zollo *et al.*, 2002).

### The Seismic Network and Data Acquisition at Mt. Vesuvius

The geophysical surveillance of Mt. Vesuvius volcano is conducted by the Osservatorio Vesuviano, which operates seismic, tiltmeter, tide-gauge, and Global Positioning System networks and performs periodical precise leveling and electronic geodimetric measurements.

The seismic activity at Vesuvius is monitored by a local seismic network consisting of 10 stations installed on the volcano edifice (Fig. 2). Seismic signals from remote stations are radiotransmitted in analog form to the surveillance center where they are digitized at a sampling rate of 100 Hz and then stored on hard disk in the Seismic Unified Data System (SUDS) format. Each seismic station is equipped with a short-period vertical component geophone (Mark L4C, 1 Hz), and the OVO station located on the volcano slope is equipped with a three-component instrument (Geotech S13, 1 Hz). The seismic network is integrated to a larger regional seismic network that is designed for detecting possible deep focus earthquakes. In addition, five digital, three-

component seismic stations equipped with short-period geophones (Mark L4-3D, 1 Hz) and local recording on digital magnetic tape at 125 samples per sec have operated almost continuously since 1987 on the volcano in order to improve the station coverage during higher seismicity periods (Fig. 2).

The OVO seismic station, installed close to the Osservatorio Vesuviano historical building at 600 m on the volcano edifice, has operated continuously since 1971. For this reason it is used to evaluate the magnitude of local earthquakes. Magnitude is inferred from the measurement of the seismogram duration according to the relationship obtained by Gruppo-Lavoro-Sismometria (1981):

$$M_D = 2.75 \log(\tau) - 2.35,$$

where  $\tau$  is the duration measured between the  $P$ -wave onset and the time when the signal-to-noise ratio is 1. This relationship has been obtained by the comparison of the records of aftershocks of the 1980 Irpinia earthquake recorded at the OVO station and on a Wood–Anderson instrument. This magnitude scale was introduced in early 1981, and in the following sections we analyze data starting from this same date.

Recently Del Pezzo and Petrosino (2001) obtained a revised duration–magnitude scale for OVO station, based on Wood–Anderson equivalent magnitude evaluated using the records obtained from digital stations.

### Earthquake Locations and Fault Mechanisms

The 3D  $P$ -wave velocity model used for earthquake location and mechanism determinations (Lomax *et al.*, 2001) is obtained by interpolation of the 2D models retrieved by nonlinear inversion of TomoVes active seismic arrival-time data.

A three-stage procedure is used to construct the 3D velocity model. First, a contour of depth for the carbonate basement top is determined along each of the 2D velocity sections by finding the deepest point at which the velocity reaches 5.0 km/sec. Second, a surface that represents the carbonate basement for the 3D model region is obtained by linear interpolation between the basement depth contours on each 2D section. A constant gradient velocity profile of  $5.5 + 0.2$  km/sec (depth 1.0 km) is assigned to all nodes of the 3D model lying below this surface. Finally, the part of the 3D model above the basement surface (the volcano-sedimentary cover and Somma–Vesuvius edifice) is formed by linear interpolation of the velocity on each 2D section. Figure 3 shows the velocity at a depth of 1 km for the final interpolated 3D velocity model of Mt. Vesuvius. The 3D interpolated model has been checked by comparing the theoretical and observed travel times from the active seismic experiments of 1994 and 1996 (Lomax *et al.*, 2001). The average travel-time residuals are 0.1 sec with a good consistency for data acquired using both the in-line and fan geometries. Earthquake locations presented in this study have

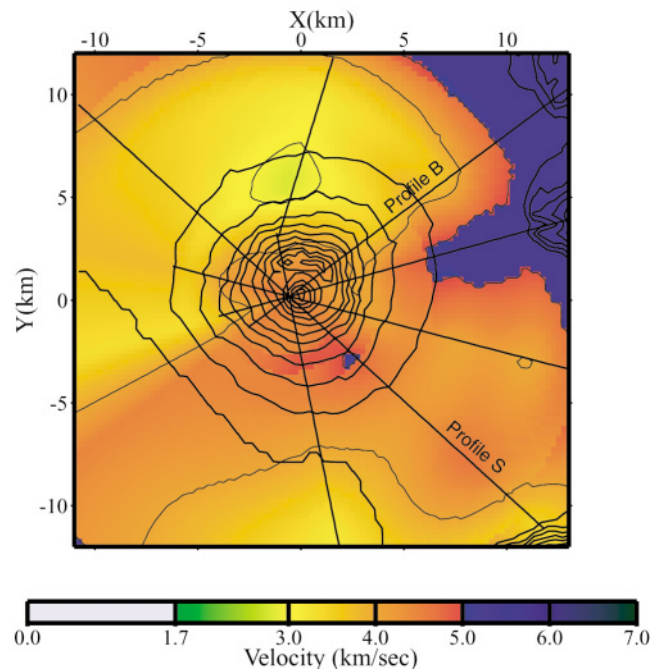


Figure 3. The interpolated 3D model shown as a horizontal section at 1-km depth. The black lines represent the active seismic profile realized in the TomoVes project. (Redrawn after Lomax *et al.*, 2001.)

been obtained with the probabilistic method proposed by Lomax *et al.* (2000), based on nonlinear optimization. The earthquake data set consists of about 400 events recorded by the permanent network during the period 1989–1998. Data collected during several temporary acquisition experiments using a digital three-component seismograph network have also been added to this database.

The earthquake locations are strongly dependant on the  $V_p/V_s$  ratio. Lomax *et al.* (2001) obtained the highest quality locations (smallest root mean square residuals) using a  $V_p/V_s$  ratio of 1.90. This relatively high value can be related to the extreme compositional heterogeneity and complexity, the presence of microfracturing, and fluids. With this  $V_p/V_s$  ratio, small residuals are obtained for the more distant stations, indicating that the 3D interpolated model well represents the lateral topographic and structural variations from the volcanic edifice through the lower, surrounding sedimentary plain to the more distant carbonate outcrops. This result is important because the correct modeling of the travel times and ray paths to the more distant stations is critical for constraining the event depths and focal mechanisms.

The earthquake locations obtained using a 3D velocity model are concentrated near the crater axis, lying both above and below the top of the carbonate basement top at about 1.8-km depth under Gran Cono (Fig. 4). The events do not show a tight clustering around the discontinuity, which excludes a significant biasing effect on the 3D locations due to the basement velocity contrast.

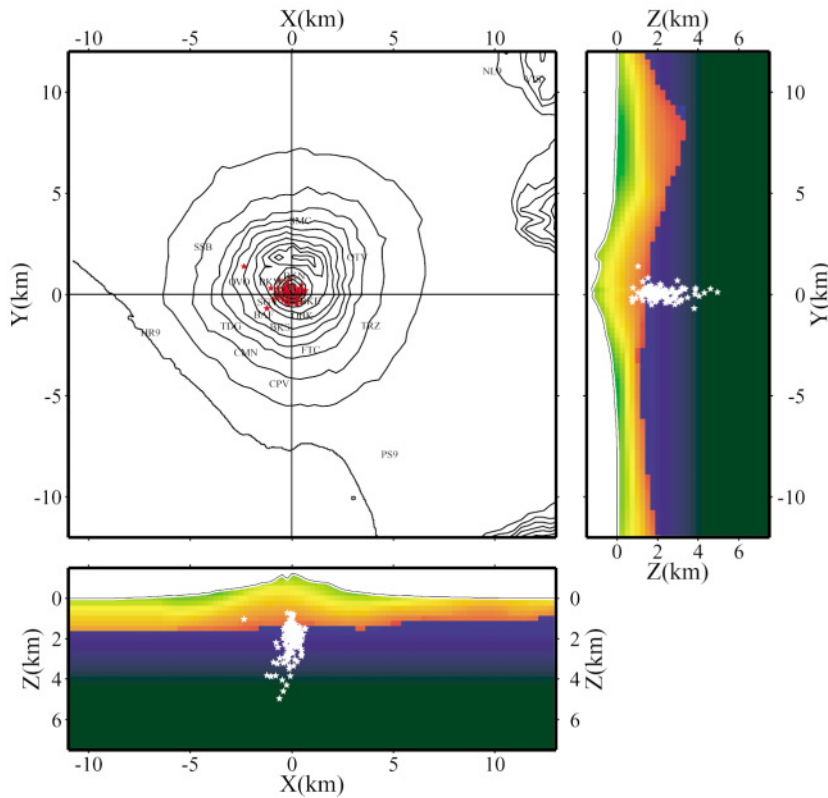


Figure 4. Earthquake location (maximum likelihood solutions) using a 3D model and a ratio  $V_p/V_s$  equal to 1.90.

### Earthquake Fault-Plane Solutions

Determination of the focal mechanism solutions and corresponding pressure ( $P$ ) and tension ( $T$ ) axes for a subset of the 1989–1999 events has been obtained by using  $P$ -wave first-motion polarities with the grid-search mechanism determination algorithm FPFIT (Reasenber and Oppenheimer, 1985). The input data used with this algorithm are the maximum likelihood hypocenter and the corresponding ray take-off angles obtained from the 3D model locations using  $V_p/V_s = 1.90$ .

The first-motion polarity data set for individual stations and the range of polarity pattern relationships between stations for different events indicate that the earthquakes at Mt. Vesuvius occur with a large variety of fault-plane solutions. Thus, we discuss here only the gross features of the distribution of  $P$  and  $T$  axes. Figure 5 shows the distribution of  $P$  and  $T$  axes for the best solutions obtained for 30 events with 10 or more first-motion observations. Although the variation in the orientation of the axes is large, they show a tendency to cluster around roughly north–south to vertical directions for the tension axes and east–southeast–west–northwest to vertical directions for the pressure axes. The orientation of the  $P$  and  $T$  axes shows no variations as a function of hypocentral depth. For a better understanding of the present stress regime, as inferred from the focal mechanisms of events beneath the volcanic complex, it is necessary to investigate in more detail the larger events for which high signal-to-noise level waveforms and information from

regional stations are available. We discuss focal mechanisms computed for the largest events that occurred during the last 10 yr in the subsequent sections.

### Time Behavior of the Seismic Activity at Mt. Vesuvius in the Last Decades

In order to evaluate a reference state for the volcano in a rest period, we need to characterize the temporal evolution of the seismicity during this time interval. For this purpose, in the next paragraphs we estimate the statistical temporal distribution of the number of events per unit time and the seismic energy released. Finally, we also report the temporal trend of the  $b$ -value of the Gutenberg–Richter law (Gutenberg and Richter, 1956), which might provide interesting insights of the evolution of the volcanic system.

### Earthquake Occurrence and Seismic Energy Released

The Mt. Vesuvius earthquake catalog contains events that occurred during the last 30 yr with duration magnitude  $M_D$  ranging from  $-0.4$  to  $3.6$ . This record corresponds to events detected by station OVO, the instrumental characteristics of which remained unchanged during the entire period of investigation. Considering instrument response and dynamic range, it is to be expected that the probability of detecting the small and large events is not constant with mag-

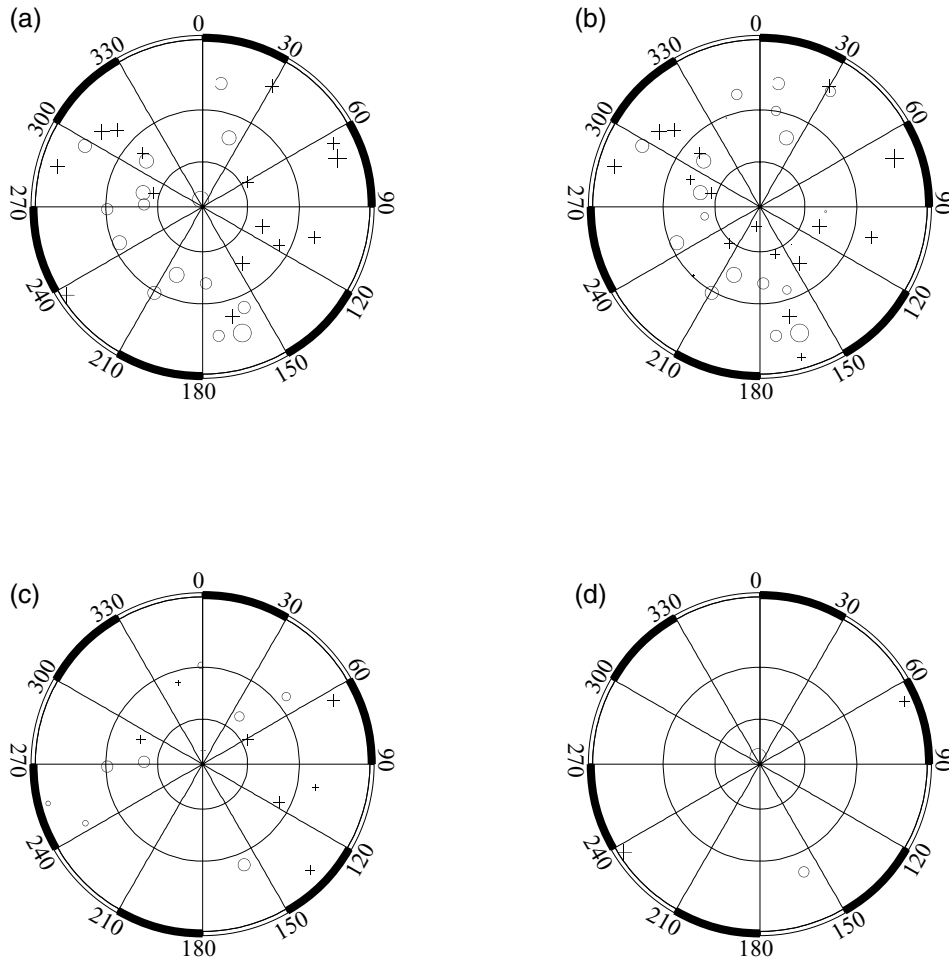


Figure 5. Stereographic views of compression (crosses) and tension (circles) axes from FPFIT first-motion mechanism determinations for (a) events with magnitude  $M \geq 2$ , (b) events with depth  $h \leq 2.5$  km, (c) events with depth  $2.5 \leq h \leq 4.0$  km, (d) events with depth  $h \geq 4.0$  km. (Redrawn after Lomax *et al.*, 2001.)

nitude, and thus the catalog completeness is not uniform. We investigated catalog completeness by analyzing the distribution of the number  $N$  of earthquakes as a function of duration magnitude (a form of the Gutenberg and Richter relationship):

$$\log(N) = a - bM_D, \tag{1}$$

where  $N$  is the number of earthquakes with magnitude  $M_D$  and  $b$  is a constant for a complete catalog. A typical effect of the incompleteness, for example incomplete detection of low-magnitude events, appears as a slope decrease in the  $\log N$  versus  $M_D$  at low magnitudes. Following standard practice, the magnitude threshold of catalog completeness is chosen at the lower magnitude for which the relation is still a straight line with a slope ( $b$ -value) of the order of one. This criterion, applied to the Mt. Vesuvius earthquake catalog, indicates the duration magnitude  $M_D$  1.9 as the minimum value for catalog completeness (Fig. 6).

In order to avoid possible inconsistencies relative to the

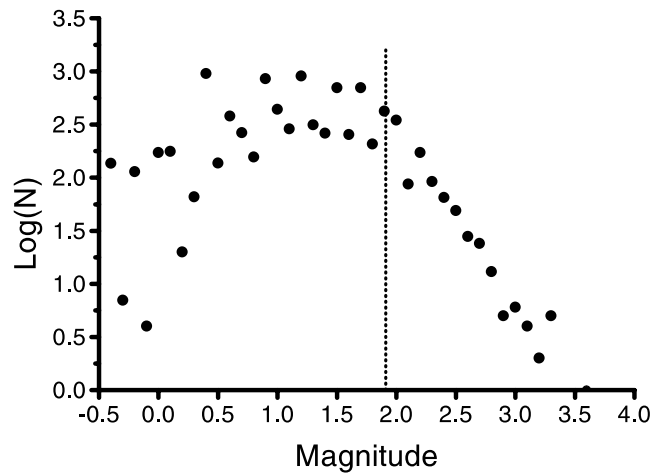


Figure 6. Earthquake number versus duration magnitude (Gutenberg and Richter relationship). The plot shows the duration magnitude  $M$  1.9 as the minimum value for catalog completeness.

older part of the catalog for which a different duration–magnitude relationship might have been used (Gruppo-Lavoro-Sismometria, 1981), we limited the analysis described subsequently to the period of time from 1 January 1981 to 31 December 1999.

The number of events and the seismic energy released are two of the most important parameters used to characterize the time evolution of the seismicity in a given area. For this purpose, we sample the total time interval considered with nonoverlapping time windows of a fixed length  $\tau$ , and then we define two stochastic variables,  $N_t(\tau)$  and  $e_t(\tau)$ , which represent, respectively, the number of events and the common logarithm of the seismic energy ( $\log(E)$ ) for each time window.

We estimate the seismic energy from magnitudes using the relationship (Gutenberg and Richter, 1956):

$$\log E = 9.9 + 1.9M_D,$$

where  $E$  is expressed in erg and  $M_D$  is the (duration) magnitude.

In Figure 7, we report the time evolution of  $N_t(\tau)$  and  $e_t(\tau)$  for different  $\tau$  during the period considered. The resulting plots show several episodes of seismicity rate at Vesuvius, as for example around the years 1989–1990. Plots, the common logarithm of the seismic energy, in contrast, show a slight linear increase with time and also periods of increased energy release corresponding to the episodes of increased seismicity rate.

The aim of the following analysis is the modeling of the earthquake occurrence using quantitative statistical approach. Different statistical approach model will be tested, and the best-fit parameters will be established. This will provide a reference quantitative model for analyzing the background volcano seismic activity. The first step in quantitatively analyzing these time series is to check their stationarity of order 1 (see, e.g., Priestley, 1981). In practice, this means testing whether the mean rate of the seismicity and the energy released are constant using a regression analysis applied to the linear model,

$$X_t = c_0 + c_1 t + \varepsilon_t, \quad (2)$$

where  $X_t$  is the variable considered, that is the number of events ( $N_t(\tau)$ ) or the common logarithm of the energy released ( $e_t(\tau)$ ),  $t$  is the time, and  $\varepsilon_t$  are the residuals. A stationary process (a constant mean rate) is characterized by  $c_1 = 0$ . Determining whether the process is stationary is important for two reasons. The first is related to the long-term linear trend defined by the parameter  $c_1$ . The second is technical: if a nonstationarity is not removed, most of the statistical techniques, used to determine the time evolution characteristics, become inapplicable (e.g., Priestley, 1981). If  $c_1$  is significantly different from zero, we detrend the time sequences through the equation

$$Y_t = X_t - (c_0 + c_1 t), \quad (3)$$

where  $Y_t$  is the detrended series and  $X_t$ ,  $c_0$ ,  $c_1$ , and  $t$  have the same meaning as in equation (1). The results are reported in Tables 1 and 2.

The variable  $N_t(\tau)$  does not show any time dependence, whereas the variable  $e_t(\tau)$  shows, in each case, a slight but statistically significant, linear increase with time ( $c_1 > 0$ ).

In the second step, after the removal of any significant trend, we try to fit a suitable statistical distribution to the variables considered. The goodness of fit is evaluated through the  $\chi^2$  test (e.g., Kalbfleisch, 1979) and through the Kolmogorov-Smirnov one-sample test (e.g., Hollander and Wolfe, 1973).

Regarding  $N_t(\tau)$ , we consider the generalized Poisson process suggested by Shlien and Toksoz (1970). Its distribution parameters are derived through the relative likelihood ratio

$$l = \prod_{i=1}^W \frac{p_q(n_i, \tau)}{f(n_i, \tau)}, \quad (4)$$

where  $p_q(n_i, \tau)$  is the theoretical probability and  $f(n_i, \tau)$  is the observed frequency of occurrence of  $n_i$  events in the time window  $\tau$ ,  $n_i$  is the number of events in the  $i$ th time window, and  $W$  is the total number of time windows. The probability  $p_q(n_i, \tau)$  is calculated with the recursive formula

$$p_q(n, \tau) = \frac{K\tau}{n} \sum_{j=0}^{n-1} (n-j)q(n-j)p_q(j, \tau), \quad (5)$$

starting with

$$p_q(0, \tau) = \exp\{-K\tau\}. \quad (6)$$

In equation (5) the function

$$q(n) = \frac{n^{-E}}{\zeta(E)} \quad (7)$$

is denoted as the Pareto law and represents the theoretical distribution of the number of grouped events, which is generally observed to have an inverse power form (e.g., De Natale and Zollo, 1986). The parameter  $E$  describes the degree of clustering of the sequence, and  $\zeta(E)$  is the Zeta-Riemann function, a normalizing factor. The generalized Poisson model assumes that the events occur grouped in time (clusters) and that the number of clusters follows a Poisson distribution (trigger model as denoted by Vere-Jones and Davies, 1966). This model differentiates from the simple Poisson process, giving a positive probability for more than one event in the time unit. The parameter  $K$  is the mean rate of cluster occurrence. The results of the fit are reported in Figure 8 for a sampling time window  $\tau$  equals 31 days, which provided  $K = 1.7$  (clusters per 31 days) and  $E = 2$ . The comparison among the observed, Poisson, and generalized Poisson distributions shows that the generalized Poisson process is a suitable model to describe the variable  $N_t(\tau)$ .

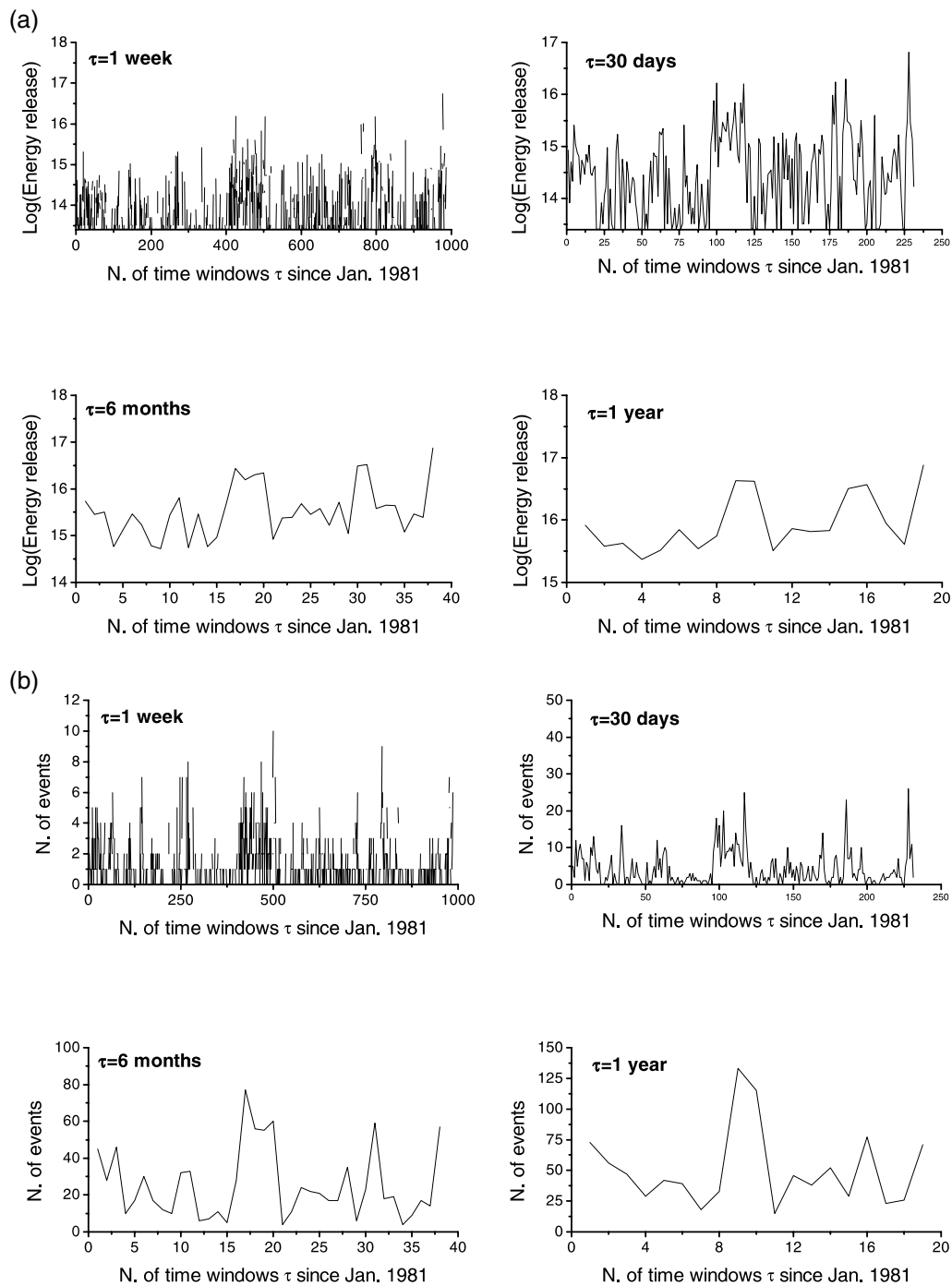


Figure 7. Time evolution of (a) energy release and (b) number of events using nonoverlapping time windows of different length ( $\tau$ ).

In order to find a statistical form of the seismic energy release, we first applied a procedure for time-trend removal. We found that the lognormal distribution (e.g., Kalbfleisch, 1979) provided a satisfactory fit to the energy data. The results, reported in Table 3, show an almost good fit for any time series with  $\tau \geq 30$  days.

### Time Behavior of the $b$ -Value

Another important indicator of the seismic activity is the  $b$ -value of the Gutenberg and Richter law. Of particular interest in studying volcanic areas is the numerical value of  $b$ ; in fact, although for nearly all the tectonic regions of the Earth  $b \leq 1.0$ , very often active volcanic areas present larger  $b$ -values (about 2.0 or more). These larger values are typical

Table 1  
Regression Analysis for  $N_i(\tau)$

$\tau$	$c_0$	$c_1$	Significance Level
7 days	$1.0 \pm 0.1$	$(-1 \pm 2) 10^{-4}$	0.54
30 days	$4.4 \pm 0.6$	$(-2 \pm 5) 10^{-3}$	0.63
6 months	$27 \pm 6$	$-0.1 \pm 0.3$	0.78
1 year	$54 \pm 15$	$0 \pm 1$	0.82

Table 2  
Regression Analysis for  $e_i(\tau)$

$\tau$	$c_0$	$c_1$	Significance Level
7 days	$14.03 \pm 0.06$	$(4 \pm 1) 10^{-4}$	<0.01
30 days	$14.4 \pm 0.1$	$(17 \pm 7) 10^{-4}$	0.02
6 months	$15.2 \pm 0.2$	$(17 \pm 8) 10^{-3}$	0.03
1 year	$15.5 \pm 0.2$	$(4 \pm 2) 10^{-2}$	0.03

for earthquake swarms, that is, the earthquake sequences without a well-defined mainshock, but with many events of approximately the same size. The most frequent explanation for high  $b$ -values is a weak crust incapable of sustaining high-strain levels and a very heterogeneous stress system, for example, due to fluid motion. This leads to a small maximum moment (or magnitude) expected for a given earthquake sequence and the occurrence of many smaller events that must accommodate the strain accumulation (e.g., Lay and Wallace, 1995).

The trend of the  $b$ -value as a function of time is estimated by calculating  $b$  through the maximum likelihood technique (e.g., Page, 1968) in overlapping time windows of 5 yr, centered each year. The error associated with the estimation of  $b$  is calculated by the following formula (Shi and Bolt, 1982):

$$\sigma(b) = \frac{2.3b^2 \sqrt{\sum (M_i - \bar{M})^2}}{N(N-1)}, \quad (8)$$

where  $M_i$  is the magnitude of the  $i$ th earthquake and  $\bar{M}$  is the average of the magnitude of the  $N$  seismic events. The results are reported in Figure 9. The plot shows a clear negative trend, ranging from  $b \approx 2$  during the 1980s to  $b \approx 1$  at the end of the investigated period. This trend is consistent with the observed increase of seismic energy with time. We note that the decrease of  $b$  with time is not constant but occurs with two major changes (end of 1980s and beginning of 1990s).

### The Largest Magnitude Events ( $M > 3$ ) of the Last 10 Years

#### Location and Fault-Plane Solutions

As inferred from the magnitude versus time analysis of the Mt. Vesuvius seismicity, the seismic energy release ap-

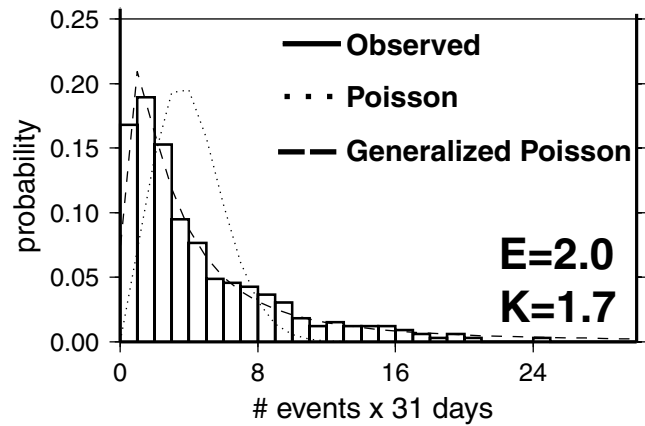


Figure 8. Comparison between Poisson (dotted line) and Generalized Poisson (dashed line) processes. The best fit shows that the Generalized Poisson process is a suitable model to describe  $N(t)$ .

Table 3  
Results of the Kolmogorov Smirnov One-Sample Test

$\tau$	Significance Level $\chi^2$ test
7 days	<0.01
30 days	>0.10
6 months	>0.10
1 year	>0.10

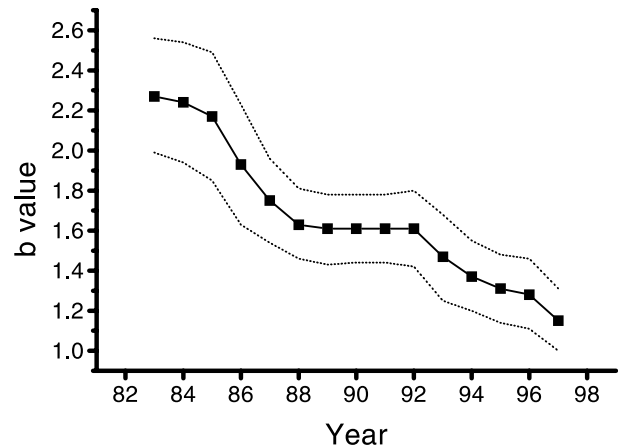


Figure 9.  $b$ -value versus time showing a clear negative trend. The dashed line represent the 95% significance level.

pears to have increased during the last decade (Fig. 7b). This increase is related to the occurrence of several  $M_D > 3$  earthquakes, accompanied by an intense swarm activity. The largest magnitude event ( $M_D$  3.6) occurred in October 1999, and it was followed 2 days later by an  $M_D$  3.1 event.

In order to investigate in detail the source characteristics (location, seismic moment, and mechanisms) we analyzed all the available seismograms of the seven largest events that

occurred at Mt. Vesuvius during the period 1989–1999 (Table 4). All these events were recorded by a minimum of one to a maximum of five near-source (distance < 6 km) Lennartz digital seismic stations equipped with three-component short-period seismometers (1-Hz).

The first  $P$  and  $S$ -arrival time and  $P$ -polarity readings were made on velocity seismic recordings. The locations of the events were obtained by integrating the digital waveform picking data set with the available picking data from the permanent network of Osservatorio Vesuviano. The events were then located using the same probabilistic procedure described in the previous section. The selected events were all located below the Mt. Vesuvius crater zone at depths less than about 4 km.

In Table 4 the earthquake depth is referred to the sea level. The  $M_D$  3.6 and  $M_D$  3.1 recent events of October 1999 have similar epicenter but depths of 4.1 and 2.3 km, respectively. According to the recent subsurface velocity models in the area, both events are located within the Mesozoic carbonate basement, but the  $M_D$  3.1 event is located just below the top of this layer. The fault-plane solutions have been obtained for six events that are shown in Table 4, using the  $P$ -polarity and the code FPFIT, whereas takeoff angles, azimuths, and distances are obtained from the 3D location. The resulting fault-plane solutions are shown in Figure 10a.

The focal mechanisms of the largest magnitude earthquakes are well constrained by the  $P$ -polarity distribution on the focal sphere. They display a clear variation in mechanism-type and nodal-plane orientation. In particular, two earthquakes (3 and 7 of Table 4) show a strike-slip mechanism with similar fault-plane orientations but opposite stress axes. Similarly, the events numbered 4 and 5 have common nodal planes but opposite stress axes. The earthquakes numbered 2 and 6 (the  $M_D$  3.6 earthquake of 9 October 1999) are associated with a dip-slip faulting mechanism with a small strike-slip component oriented approximately in the east-west direction.

The occurrence of non-double-couple mechanisms in volcanic fields is associated with fluid-/gas-driven rock fracturing and is usually investigated by the moment tensor analysis of moderate size earthquake waveforms. Among the largest magnitude events analyzed in this study, the  $M_D$  3.6 earthquake that occurred on 9 October 1999 was the only

one for which the number, quality, and azimuthal distribution of digital recordings allowed the accurate evaluation of a moment tensor solution. The moment tensor components were determined using the first  $P$  and  $S$  pulse amplitudes assuming a point source mechanism (De Natale and Zollo, 1989).

The moment tensor analysis was performed firstly considering a seismic source with no volume change; this is obtained by constraining the moment tensor to have zero trace. In this case, the ratio  $\varepsilon$  between the smallest ( $\lambda_{\min}$ ) and

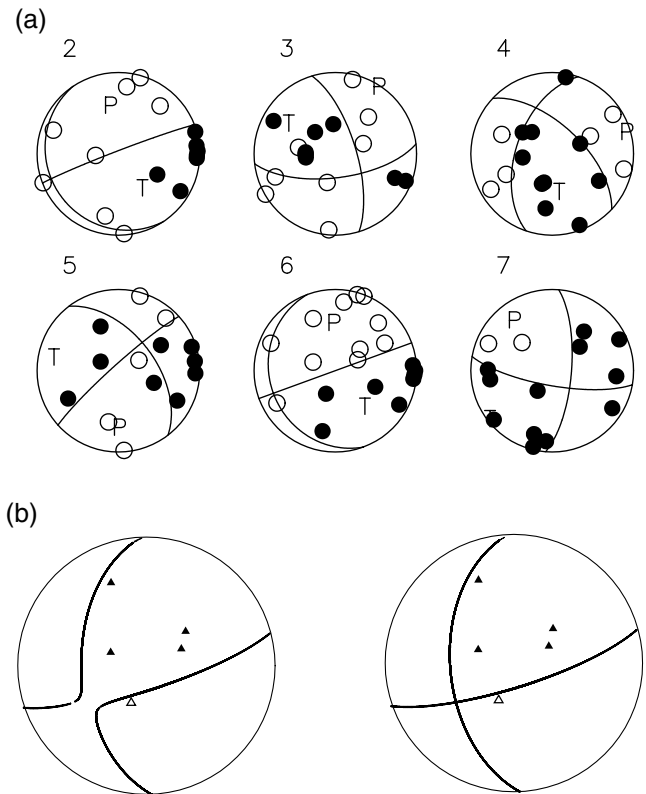


Figure 10. (a) Stereographic projection of fault-plane solution for the events 2–6 of Table 4. Filled circles represent compression. (b) Moment tensor solution of the event that occurred on 9 October 1999. The figure shows the zero-trace and double-couple solutions.

Table 4  
Source Parameters of Events with  $M > 3$

Event Number	Date (dd/mm/yy)	Latitude (°)	Longitude (°)	Depth (km)	$M_D$	$M_0^P$ (N m)	$M_0^S$ (N m)	$r$ (m)	$\Delta\sigma$ (MPa)
1	19/03/89	40.8250	14.4244	1.29	3.3	$6.1 \pm 6.5 \times 10^{13}$	$8.7 \pm 0.8 \times 10^{13}$	160	9.2
2	16/09/95	40.8185	14.4255	3.08	3.2	$1.9 \times 10^{13}$	$2.1 \times 10^{13}$	185	1.5
3	24/09/95	40.8200	14.4251	1.63	3.1	$3.2 \pm 0.6 \times 10^{13}$	$3.0 \pm 0.3 \times 10^{13}$	193	1.8
4	25/04/96	40.8226	14.4284	1.04	3.3	$2.6 \pm 0.5 \times 10^{13}$	$6.4 \pm 0.5 \times 10^{13}$	205	3.3
5	05/11/97	40.8213	14.4270	3.88	3.0	$1.8 \pm 1.3 \times 10^{13}$	$2.3 \pm 1.0 \times 10^{13}$	196	1.4
6	09/10/99	40.8095	14.4192	4.12	3.6	$1.3 \pm 0.6 \times 10^{14}$	$1.6 \pm 0.5 \times 10^{14}$	260	4.0
7	11/10/99	40.8201	14.4231	2.34	3.1	$2.0 \pm 1.1 \times 10^{13}$	$2.3 \pm 0.5 \times 10^{13}$	145	3.3

Table 5  
Moment Tensor Solution for the 9 October 1999  $M_D$  3.6 Earthquake

	Principal Axes									
	Eigenvalues				$\varepsilon$	Eigenvector Components				
	max	inter	min	$\phi$ (°)		$\delta$ (°)	$\phi$ (°)	$\delta$ (°)	$\phi$ (°)	$\delta$ (°)
Tr(0)	1.00	-0.01	-0.98	0.01	129.4	18.1	24.8	37.6	239.8	46.8
DC	1.00	0.00	-1.00	—	129.0	17.9	24.5	37.8	239.1	46.7

the largest ( $\lambda_{\max}$ ) eigenvalue of the moment tensor ( $\varepsilon = |\lambda_{\min}|/|\lambda_{\max}|$ ) is a measure of the deviation of the seismic source from the double-couple mechanism (Dziewonski and Woodhouse, 1983). For a pure double-couple source,  $\varepsilon = 0$ , and  $\varepsilon = 0.5$  in the case of a compensated linear vector dipole (CLVD) source (Knopoff and Randall, 1970). Secondly, the further constraint of a moment tensor with zero determinant has been applied to evaluate the best double-couple solution. Table 5 reports the obtained results.

Tr(0) and DC are for zero-trace and pure double-couple solutions, respectively, and  $\phi$  and  $\delta$  are the azimuth and plunge of axis orientations.

The moment tensor solution for the Tr(0) solution shows a very small value for the ratio  $\varepsilon$  ( $\varepsilon = 0.01$ ) indicating a moment tensor solution not significantly different from a pure double-couple source mechanism. Moreover, the principal axes obtained for the Tr(0) and DC solutions are very similar, showing that a double-couple solution is obtained also without constraining the moment tensor to have zero trace and determinant. Figure 10b also shows the computed nodal planes referred to Tr(0) and DC solutions. As indicated in Table 5 they are very similar, the difference being a minimum non-double-couple component of the Tr(0) solution. Thus we conclude that the earthquake of  $M_D$  3.6 that occurred on 9 October 1999 does not show a significant non-double-couple component in the moment tensor. In addition, the inferred fault-plane solution is very similar to that obtained by using only  $P$ -wave polarities, with the exception of a slightly larger strike-slip component present in the moment tensor solution.

### Seismic Moments and Source Radii

We calculated scalar seismic moment of the selected events by using the following relationship (Aki and Richards, 1980):

$$M_o^{P,S} = \frac{4\pi\rho_o^{1/2}\rho_x^{1/2}v_o^{5/2}v_x^{1/2}\Omega_o^{P,S}R}{F^S R_{\phi\phi}^{P,S}}$$

where  $\rho_o$ ,  $v_o$ ,  $\rho_x$ ,  $v_x$ , are density and  $P$  (or  $S$ ) velocity at the source and receiver regions, respectively,  $F$  is the free surface amplification effect,  $R$  is the hypocentral distance, and  $R_{\phi\phi}^{P,S}$  is the radiation pattern coefficient. The values used for parameters in the previous formula are given in Table 6.

The values for velocities and densities are inferred from the tomographic study of Zollo *et al.* (2000), and  $S$ -wave

Table 6  
Parameters Used for Seismic Moment Calculations

		$P$	$S$
$\rho_o$ (kg/m <sup>3</sup> )	Density at source	2700	2700
$\rho_x$ (kg/m <sup>3</sup> )	Density at receiver	2400	2400
$v_o$ (m/sec)	Velocity at source	6000	3150
$v_x$ (m/sec)	Velocity at receiver	2000	1050
$F^S$	Free surface coefficient	2	2
$R_{\phi\phi}^{P,S}$	Radiation coefficient	0.52	0.63

velocity is obtained by using  $V_p/V_s = 1.9$  as suggested by the work of Lomax *et al.* (2001).

The seismic moment  $M_0$  for each event (see Table 4) was computed by averaging the low-frequency  $P$ - and  $S$ -displacement-spectrum level over the ground-motion components and stations. Each spectrum was computed using a 3-sec window containing the selected phase and was corrected for the instrumental response. A preliminary analysis of the anelastic attenuation on the recorded spectra showed that this effect is negligible due to the rather short propagation distances (<5–7 km).

Figures 11 and 12 show an example of seismograms and displacement spectra for the largest magnitude earthquake that occurred on 9 October 1999. Interestingly, the displacement spectra corrected for the geometrical spreading to each station are fairly consistent, which validate the used correction for the geometrical and anelastic attenuation.

The computed seismic moments for  $P$  and  $S$  waves with the relative uncertainty are reported in Table 4.

The seismic moment estimates inferred from  $P$ -wave arrivals are affected by a greater uncertainty due to the possible effect of secondary phases with relevant amplitude in the selected time window.

The source radii of these events were estimated by using the Brune (1970) relationship ( $r = 0.37\beta/f_c$ ;  $\beta$  is the shear-wave velocity and  $f_c$  is the corner frequency), whereas the static stress drop is obtained by the Keilis-Borok (1959) formula ( $\Delta\sigma = 7/16 M_o/r^3$ ). The inferred source radii and stress-drop values are also reported in Table 4 and plotted in Figure 13 as a function of seismic moment. With the exception of the 1989 event, the largest magnitude earthquakes of this last decade follow an approximate constant stress-drop scaling moment interval, with a value around 1.5–4 MPa. Due to the uncertainties of the moment and corner frequency

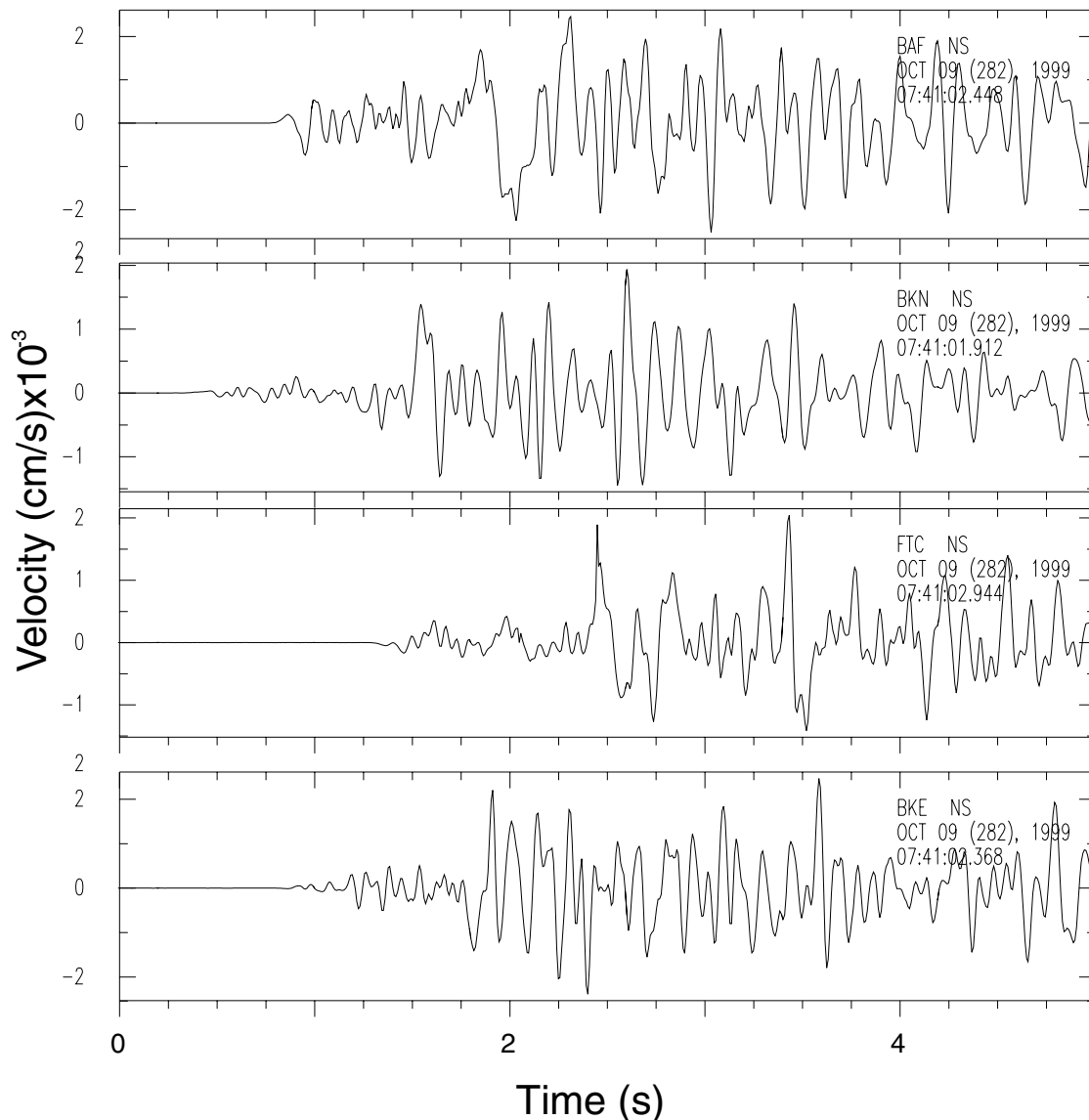


Figure 11. Examples of velocity records of the 9 October 1999 earthquake at four digital stations.

measurements, the error on stress drops are of the order of 50% or more of the estimated values.

### Discussion and Conclusions

In this article we analyze the space and time behavior of seismicity at Mt. Vesuvius during the last two decades with the main objective of updating and characterizing the seismic regime of the volcano during the present quiescent period of volcanic activity. For this purpose we have incorporated the new results on the volcano structure inferred from active seismic tomography experiments, the newly implemented 10-yr arrival time catalog, and a high-quality digital waveform data set for  $M > 3$ .

About 400 selected microearthquakes with duration

magnitudes ranging from 1 to 3.6 have been located using a 3D discontinuous velocity model of Mt. Vesuvius and surrounding Campanian plain interpolated from the 2D models obtained from the nonlinear inversion of active seismic data (Zollo *et al.*, 2000; Lomax *et al.*, 2001).

The location method is based on the travel-time computation by the finite-difference solution of the eikonal equation and a probabilistic approach for the estimate of source location parameters. It is specifically designed to locate events in heterogeneous structures like Mt. Vesuvius, which exhibits a rough topography, a strong lateral variation of the velocity field both inside and outside of the volcano edifice, and a well-defined velocity discontinuity separating the shallow volcanic/alluvium sediments from the Mesozoic carbonate basement.

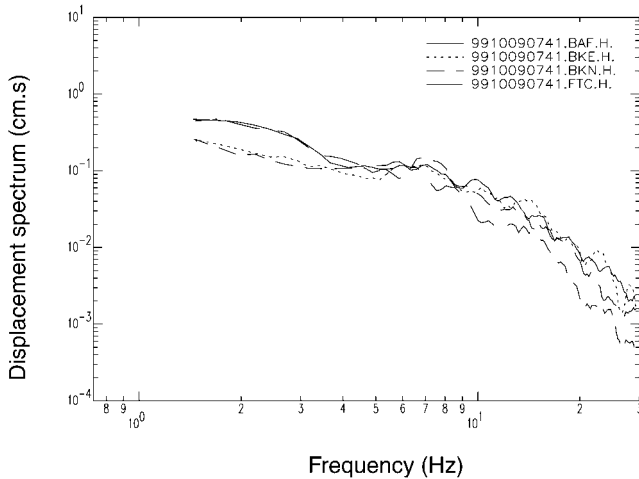


Figure 12. Examples of displacement spectra of the 9 October 1999 earthquake. The spectra, corrected for the geometrical spreading, are fairly consistent.

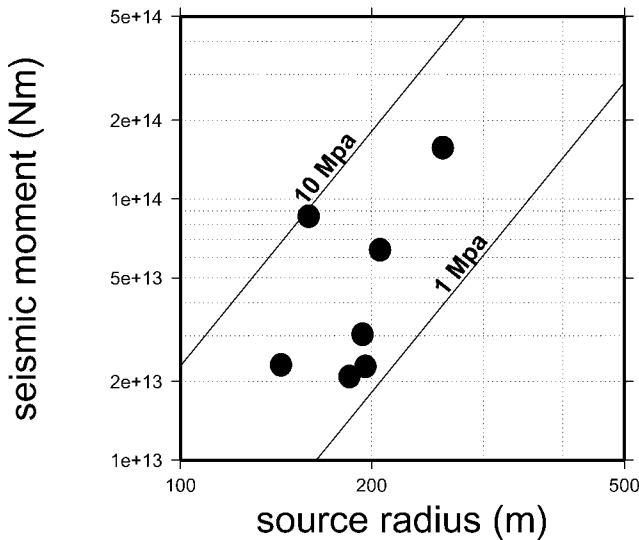


Figure 13. Seismic moment versus Brune source radius for the analyzed events.

In Figure 14 the microearthquake epicenters are plotted on the 2D tomographic models for profiles B and S (see Fig. 3 for their locations on map). The 2D tomographic images show a sharp  $P$ -velocity discontinuity at a depth range of 2000–3000 m depth below sea level underneath the volcano that corresponds to the carbonate basement top. The limestone top appears to have an irregular shape and generally dips from the edges of the Campanian Plain toward the volcano. This trend is also consistent with the Bouguer anomalies pattern (Cassano and La Torre, 1987; Berrino *et al.*, 1998). The relocated seismicity appears concentrated near and beneath the Mt. Vesuvius crater, with depths lying above and below the interface, which marks the carbonate basement top. The location of background seismicity at Mt. Ve-

suvius suggests an important role played by the lithological/mechanical transition between the volcanic deposits and Carbonate Mesozoic sequences in deformation and fracturing processes occurring inside and beneath Mt. Vesuvius during the present quiescent phase of the volcano. The axial cone earthquake distribution at depths of 1500–3500 m below sea level can be attributed to the concurrent effects of the shear stress increase around the zone, where the largest change in rock rigidity is expected, that is, the carbonate top discontinuity and the rock strength weakening due to the dense fracturing associated to magma ascent to the surface during the eruption episodes.

The focal mechanisms of microearthquakes from the last decade show no clear patterns of stress-axis orientation as a function of depth, although there is evidence for a clustering around roughly the north–south to vertical directions for the tension axes and east-southeast–west-northwest to vertical directions for the pressure axes. Based on the computation of focal mechanism for 30 Mt. Vesuvius events, Bianco *et al.* (1998) recognized two main orientations of  $P$  and  $T$  axes. The directions found in this study are consistent with one of the two proposed trends.

Based on numerical simulations of the stress distribution inside and beneath Mt. Vesuvius due to local and regional stress sources, Russo *et al.* (1997) suggested that a shear stress increase is expected around the structural discontinuity represented by the carbonate top, in response to symmetric tensional or strike-slip regional stress regimes. This effect could be amplified nearby the crater axis due to the additional stress increment related to the topographic relief of the volcano edifice. The calculated orientations of principal stresses in this model would favor near vertical, normal fault earthquakes (horizontal  $T$  and vertical  $P$  axes), in contrast with results from the present study, which show variable plunges (from near vertical to horizontal) of  $P$  and  $T$  axes and no dominant normal-faulting mechanism. The possible irregular, faulted shape of the carbonate top discontinuity underneath the volcano complex could explain this discrepancy since the shear stress orientations nearby the discontinuity would strongly depend on its morphology. De Natale *et al.* (2000) performed a finite-element modeling to simulate the stress field due to a gravitational body force in an axisymmetric volcano characterized by a central high-rigidity anomaly, including the action of a constant regional stress. In their model the effect of the high-rigidity body is to concentrate shear stresses at its borders, which can reach the rock failure threshold. According to this numerical simulation dominant normal-faulting pattern is expected for Mt. Vesuvius microearthquakes, consistent with results obtained by Russo *et al.* (1997).

Based on a high-quality waveform data set, we analyzed in detail the location, mechanism, moment, and fracture size of the largest  $M_D > 3$  events that occurred during the last decade. The events are located in the same area and depth range of the whole seismicity, and their fault-plane solutions also show variable stress-axis and nodal-plane orientations.

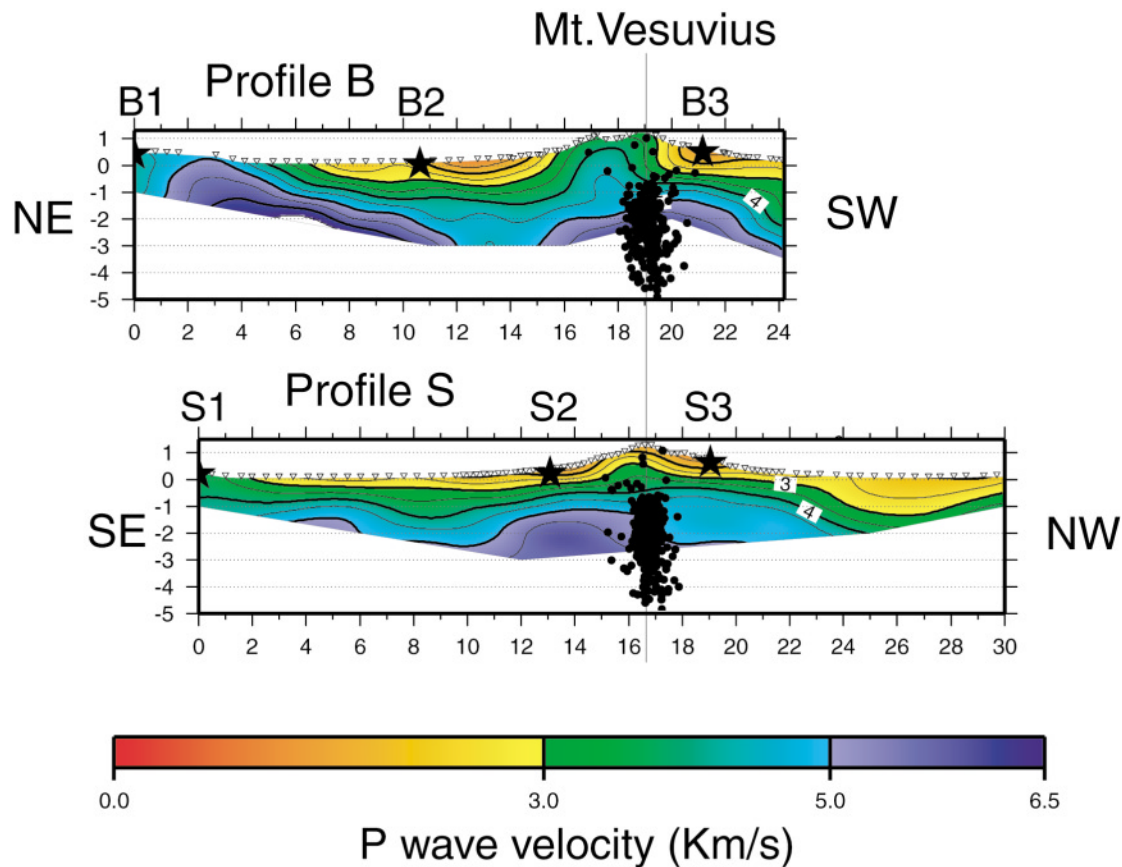


Figure 14. Hypocentral location superimposed on the tomographic velocity model along Profile B and S (see Fig. 3).

The availability of a sufficient number of high-quality digital waveforms for the  $M_D$  3.6 earthquake that occurred on 9 October 1999 enabled us to estimate the moment tensor solution of this event, based on amplitudes of the first  $P$  and  $S$  pulses and takeoff angles computed from the earthquake location in the 3D medium. This analysis showed no significant departure of the fault mechanism from a pure shear, double-couple source as inferred from the comparison of the zero-trace and double-couple moment tensor solutions. A similar analysis could not be applied to other events in the available data set because of the poor station coverage or insufficient number of recordings.

With the exception of the 1989 event, the largest magnitude earthquakes of the last decade follow an approximate constant stress-drop (average value of 1.5–4 MPa) scaling of seismic moment with source radius. A near-constant stress-drop scaling has also been observed in other volcanic areas (e.g., Campi Flegrei caldera) (Del Pezzo *et al.*, 1987), which suggests that the mechanism causing worldwide high-frequency cutoff of seismic spectra (either a path or source effect) could be different in volcanic rock environment.

The analysis of the seismic catalog (origin time and magnitude) focused on the temporal evolution and statistical

distribution of some variables, such as the temporal distribution of events, the seismic energy released, and the  $b$ -value. In particular, the analysis of the temporal occurrence of the events supports the observation of Bonasia *et al.* (1985) that the earthquake occurrence at Mt. Vesuvius follows a generalized Poisson statistic, which indicates the tendency of microearthquakes to occur clustered in time. The parameter, which describes the clustering degree, is the exponent  $E$  of the “Pareto law” (see equation 7) that has a value of 2 for the Mt. Vesuvius catalog. The parameter  $E$  generally assumes values in the range 1.5–4 in different tectonic and volcanic areas of the world (De Natale and Zollo, 1986). Smallest values of  $E$  (close to 2), observed in volcanic areas, indicate a dominant tendency of earthquake to occur grouped in time (swarm-type behavior).

The most relevant result of this temporal analysis of seismicity at Mt. Vesuvius is the evidence for an increase with time of the average seismic energy released during the last two decades. This is consistent with the sharp decrease in the  $b$ -value during the same period. We argue that these two parameters are not independent: the variation of the parameter  $b$  from values  $\approx 2$  typical of volcanic areas (e.g., Lay and Wallace, 1995) to values  $\approx 1$  that usually charac-

terized tectonic areas, tends to increase the maximum magnitude expected for the seismic events; therefore, as a consequence, also the seismic energy release tends to increase.

The variations of fluid pore pressure related to hydrothermal fluid circulation induced by natural or industrial activity is one of the possible causes for temporal change in earthquake magnitude distribution in volcanic areas. Evidence for fluid presence at Mt. Vesuvius is contained in seismic data and magnetotelluric and geoelectric soundings (Di Maio *et al.*, 1998; Ventura and Vilardo, 1999), as well as the presence of intense fumarolic activity at the volcano surface. In parallel with changes in seismic energy release, the temperature measured at the fumaroles has decreased to about 300°C since the end of the last eruption, which took place in 1944 (Chiodini *et al.*, 2002). The cooling of the hydraulic system could have induced a substantial drop in fluid pressure, thus affecting the fault mechanics and seismicity occurrence and distribution in the area. The influence of decreasing fluid pressure on seismicity patterns has been recently investigated by Nielsen *et al.* (2000), who simulated numerically the expected fracture pattern in 2D lattices by varying the level of initial fluid pressure. They generated random distributions of frictional properties and found that the fracture episodes are triggered and propagated in the lattice by changing fluid-pressure levels. The results of these simulations show that a change in the distribution of the number of events as a function of moment is expected for variations of the fluid-pressure level. In particular, an increase in the number of larger size events relative to smaller ones is observed when the fluid pressure in the system is decreased.

These numerical experiments would therefore suggest a dominant effect of fluid pressure variations on the present seismic regime at Mt. Vesuvius, which could be driven by the progressive cooling of the volcanic system.

### Acknowledgments

We gratefully acknowledge David Hill, who carefully read the manuscript and gave valuable suggestion to improve the quality of the article. This article was partially supported by GNV-INGV (PQ 2000–2002).

### References

- Aki, K., and P. Richards (1980). *Quantitative Seismology: Theory and Methods*, Freeman, San Francisco.
- Arnò, V., C. Principe, M. Rosi, R. Santacroce, A. Sbrana, and M. Sheridan (1987). Eruptive history, in *Somma–Vesuvius*, R. Santacroce (Editor), CNR Editions, Rome, 53–103.
- Auger, E., P. Gasparini, J. Virieux, and A. Zollo (2001). Seismic evidence of an extended magmatic sill under Mt. Vesuvius, *Science* **294**, 1510–1512.
- Berrino, G., G. Corrado, and U. Riccardi (1998). Sea gravity data in the gulf of Naples: a contribution to delineating the structural pattern of the Vesuvian area, *J. Volc. Geotherm. Res.* **82**, 139–150.
- Bianco, F., M. Castellano, G. Milano, G. Ventura, and G. Vilardo (1998). The Soma–Vesuvius stress field induced by regional tectonics: evidences from seismological and mesostructural data, *J. Volc. Geotherm. Res.* **82**, 199–218.
- Bonasia, V., E. Del Pezzo, F. Pingue, R. Scandone, and R. Scarpa (1985). Eruptive history, seismic activity and ground deformation at Mt. Vesuvius, Italy, *Ann. Geofis.* **3**, 395–406.
- Brune, N. (1970). Tectonic stress and the spectra of seismic shear waves, *J. Geophys. Res.* **75**, 4997–5009.
- Bruno, P., G. Cippitelli, and A. Rapolla (1998). Seismic study of the mesozoic carbonate basement around Mt. Soma–Vesuvius, Italy, *J. Volc. Geotherm. Res.* **84**, 311–322.
- Cassano, E., and P. La Torre (1987). Geophysics, in *Somma–Vesuvius*, R. Santacroce (Editor), CNR Editions, Rome, 175–196.
- Chiodini, G., L. Marini, and M. Russo (2002). Geochemical evidence for the existence of high-temperature hydrothermal brines at Vesuvio volcano (Italy), *Geochem. Cosmochim. Acta* (in press).
- De Matteis, R., D. Latorre, A. Zollo, and J. Virieux (2000). 1D P-velocity models of Mt. Vesuvius volcano from the inversion of tomographic first arrival time data, *Pageoph* **157**, 1643–1661.
- De Natale, G., and A. Zollo (1986). Statistical analysis and clustering features of the phlegraean fields earthquake sequence (May 1983–May 1984), *Bull. Seism. Soc. Am.* **76**, 801–814.
- De Natale, G., and A. Zollo (1989). Earthquake focal mechanisms from inversion of first P and S wave motion, in *Digital Seismology and Fine Modeling of the Lithosphere*, R. Cassinis, G. Nolet, and G. Panza (Editors), Plenum, New York, 399–419.
- De Natale, G., S. M. Petrazzuoli, C. Troise, F. Pingue, and P. Capuano (2000). Internal stress field at Mount Vesuvius: a model for background seismicity at a central volcano, *J. Geophys. Res.* **105**, 16,207–16,214.
- Del Pezzo, E., and S. Petrosino (2001). A local-magnitude scale for Mt. Vesuvius from synthetic Wood–Anderson seismograms, *J. Seismology* **5**, 207–215.
- Del Pezzo, E., G. De Natale, M. Martini, and A. Zollo (1987). Source parameters of microearthquakes at Phlegraean Fields (southern Italy) volcanic area, *Phys. Earth Planet. Interiors* **47**, 25–42.
- Di Maio, R., P. Mauriello, D. Patella, Z. Petrillo, S. Piscitelli, and A. Siniscalchi (1998). Electric and electromagnetic outline of the Mount Soma–Vesuvius structural setting, *J. Volc. Geotherm. Res.* **82**, 219–238.
- Dziewonski, A., and J. Woodhouse (1983). An experiment in systematic study of global seismicity: centroid-moment solutions for 201 moderate and large earthquakes of 1981, *J. Geophys. Res.* **88**, 3247–3271.
- Fedi, M., G. Florio, and A. Rapolla (1998). 2D modelling of Somma–Vesuvius structure by aeromagnetic data, *J. Volc. Geotherm. Res.* **82**, 239–247.
- Finetti, I., and C. Morelli (1974). Esplorazione sismica a riflessione dei golfi di napoli e pozzuoli, *Boll. Geofis. Teor. Appl.* **16**, 122–175.
- Gasparini, P., and TomoVes Working Group (1998). Looking inside Mt. Vesuvius, *EOS* **79**, 229–232.
- Gruppo-Lavoro-Sismometria (1981). Il terremoto irpino del 23 novembre 1980, *Rend. Soc. Geol. It.* **4**, 427–450.
- Gutenberg, B., and C. Richter (1956). Earthquake magnitude, intensity, energy, and acceleration, *Bull. Seism. Soc. Am.* **46**, 105–145.
- Hollander, M., and D. Wolfe (1973). *Nonparametric Statistical Methods*, Wiley, New York.
- Kalbfleisch, J. (1979). *Probability and Statistical Inference*, Springer-Verlag, New York.
- Keilis-Borok, W. I. (1959). On the estimation of the displacement in an earthquake source and of source dimension, *Ann. Geof.* **12**, 205–214.
- Knopoff, L., and M. Randall (1970). The compensated linear-vector dipole: a possible mechanism for deep earthquakes, *J. Geophys. Res.* **75**, 4957–4963.
- Lay, T., and T. Wallace (1995). *Modern Global Seismology*, Academic, San Diego.
- Lomax, A., J. Virieux, P. Volant, and C. Berge (2000). Probabilistic earthquake location in 3D and layered models: introduction of a Metropolis–Gibbs method and comparison with linear locations, in *Advances in Seismic Event Location*, C. Thurber and N. Rabinowitz (Editors), Kluwer, Amsterdam, 101–134.

- Lomax, A., A. Zollo, P. Capuano, and J. Virieux (2001). Precise, absolute earthquake location under Somma–Vesuvius volcano using a new 3D velocity model, *Geophys. J. Int.* **146**, 313–331.
- Mc Nutt, S. R. (1996). Seismic monitoring and eruption forecasting of volcanoes: a review of the state-of-the-art and case histories, in *Monitoring and Mitigation of Volcano Hazard*, R. Scarpa and R. Tilling (Editors), Springer-Verlag, New York, 99–146.
- Muller, M., A. Hordt, and F. Neubauer (1999). Electromagnetic technique's success at Vesuvius points to use in forecasting eruptions, *EOS* **20**, 393–401.
- Nielsen, S., A. Zollo, and W. Marzocchi (2000). Change of seismicity inside Mt. Vesuvius: cooling of the fluid system? in *17th Course: Fault Interaction by Stress Transfer: New Horizons for Understanding Earthquake Occurrence*, M. Cocco, R. Stein, and J. Rice (Editors), International School of Geophysics, Erice.
- Page, R. (1968). Aftershocks and microaftershocks of the great Alaska earthquake of 1964, *Bull. Seism. Soc. Am.* **58**, 1131–1168.
- Priestley, M. (1981). *Spectral Analysis and Time Series*, Vols. 1 and 2, Academic, New York.
- Principe, C., M. Rosi, R. Santacroce, and A. Sbrana (1987). Geophysics, in *Somma–Vesuvius*, R. Santacroce (Editor), CNR Editions, Rome, 11–52.
- Reasenber, P., and D. Oppenheimer (1985). FPFIT, FPLOT, and FPPAGE: FORTRAN computer programs for calculating and plotting earthquake fault-plane solutions, *U.S. Geol. Surv. Open-File Rept.* 85-739, 1109.
- Russo, G., G. Giberti, and G. Sartoris (1997). Numerical modeling of surface deformation and mechanical stability of Vesuvius volcano, Italy, *J. Geophys. Res.* **102**, 24,785–24,800.
- Santacroce, R. (1991). Prospects for the determination of the magma chamber parameters of Vesuvius based on the petrological and vulcanological data, in *Prospects for the Simulation of Volcanic Eruptions*, F. Dobran and F. Mulargia (Editors), Editions Giardini, Pisa, 91–115.
- Scandone, R., L. Giacomelli, and P. Gasparini (1993). Mount Vesuvius: 2000 years of volcanological observation, *J. Volc. Geoth. Res.* **58**, 5–25.
- Shi, Y., and B. Bolt (1982). The standard error of the magnitude frequency b value, *Bull. Seism. Soc. Am.* **72**, 1677–1687.
- Shlien, S., and M. Toksoz (1970). A clustering model for earthquake occurrence, *Bull. Seism. Soc. Am.* **60**, 1765–1787.
- Ventura, G., and G. Vilardo (1999). Seismic-based estimate of hydraulic parameters at Vesuvius, *Geophys. Res. Lett.* **26**, 887–890.
- Vere-Jones, D., and R. Davies (1966). A statistical survey of earthquakes in the main seismic region of New Zealand. II. Time series analysis, *N. Zealand J. Geol. Geophys.* **9**, 251–284.
- Zollo, A., L. D'Auria, R. De Matteis, A. Herrero, and P. Gasparini (2002). Bayesian estimation of 2-d p-velocity models from active seismic arrival time data: imaging of the shallow structure of Mt. Vesuvius (southern Italy), *Geophys. J. Int.* (submitted for publication).
- Zollo, A., R. De Matteis, L. D'Auria, and J. Virieux (2000). A 2-d non linear method for travel time tomography: application to Mt. Vesuvius active seismic data, in *Problems in Geophysics for the Next Millennium, ING-Editrice Compositori, Bologna*, E. Boschi, G. Ekstrom, and A. Morelli (Editors), 125–140.
- Zollo, A., P. Gasparini, J. Virieux, H. Le Meur, G. De Natale, G. Biella, E. Boschi, P. Capuano, R. de Franco, P. Dell' Aversana, R. De Matteis, I. Guerra, G. Iannaccone, L. Mirabile, and G. Vilardo (1996). Seismic evidence for a low velocity zone in the upper crust beneath Mount Vesuvius, *Science* **274**, 592–594.

Dipartimento di Scienze Fisiche  
Università di Napoli  
"Federico II"  
Naples, Italy  
(A.Z.)

Osservatorio Vesuviano  
INGV, Napoli  
Naples, Italy  
(W.M., P.C., G.I.)

GeoScience Azur  
Nice, France  
(A.L.)

Manuscript received 1 December 2000.